proposed for motion compensation in neuroimaging [1–7]. In cardiac PET studies, effects of wall contractile and respiratory motion can be smoothed in the temporary sampled PET images, but global movement of the patients during the relatively long scanning period is still a significant source of errors [8–11].

It was shown that misalignment by a 20-mm shift in the lateral/septal direction between transmission and ^{18}F-fluorodeoxyglucose (^{18}FDG) emission scans caused a 30% change in regional activity in cardiac ^{18}F-FDG PET [8]. To align two ^{18}F-FDG emission images acquired on different days, Bacharach et al. [11] proposed a registration technique based on the rigid body model using the transmission images by assuming no misregistration between transmission and emission data sets.

Cardiac ^{15}O-water PET studies provide quantitative information with regard to the viabilities of myocardium using the myocardial blood flow (MBF), coronary flow reserve, and perfusable tissue index [12–19]. Naum et al. [20] demonstrated that the movement occurred during dynamic scans with cycling. They proposed a method to correct for the motion during a single dynamic scan, and among different sessions, by aligning the dynamic frames of ^{15}O-water images using two external radioactive markers placed on the back of a subject. Although their technique did not provide correction for misalignment between transmission and emission data, reasonable improvement in calculated MBF values was demonstrated.

Correcting the misalignment between the transmission and emission data is a challenging task because the image contrast of transmission images differs from that of emission images. The distribution of ^{15}O-water also varies dramatically in regions of the right and left ventricles, myocardium, and other organs over time. Additionally, the image quality of PET with ^{15}O-water is worse than that with other radioligands due to the short half life of ^{15}O, which makes image registration difficult.

In this paper, we describe a novel approach using an optical motion-tracking system for detecting the subject's global movement during the relatively long study period, as an extension of the early studies of Watabe et al. [4]. The proposed technique provided correction for misalignment between dynamic emission sinograms, and also provided accurate attenuation correction, in which misalignment between attenuation map and each emission sinogram was corrected in the reconstruction stage.

First, the inherent accuracy of our system was evaluated. Then, the system was validated on a cardiac phantom study for artificial misalignment between an attenuation map and emission data. Correction for global movement obtained by monitoring the locations of external markers on chest skin was validated in a ^{15}O-water cardiac PET study in a healthy volunteer at rest.

Materials and methods

Hardware-based position monitoring system

To detect motion of a subject, we adopted an optical motion-tracking device in which targets attached to the chest skin are monitored. The motion compensation approach using an optical motion-tracking system has been previously validated in brain PET studies [3–7]. We applied this approach to the cardiac PET studies. Figure 1a shows an optical motion-tracking system, POLARIS (Northern Digital Inc., Canada). The POLARIS has two charge-coupled-device cameras, and provides the 3D position of a target. The three-dimensional position is measured in the form of 6 degrees of freedom: three rotational angles, and three translational directions. The manufacturer reports that the accuracy of the rotational angle and translation are better than 0.3° and 0.5 mm, respectively. Figure 1b shows a target with four infrared-reflective markers and supporting post. The target and supporting post made of carbon resin were pinned with two fluoroplastic screws. Figure 1c shows the position calibration tool used to convert the locations of subject positions in the POLARIS coordinate into PET coordinates. Figure 1d represents the schematic diagram of our system. Locations of targets attached to the chest skin of the subject and the gantry of a PET scanner were measured with the POLARIS. The target on the gantry of the PET scanner was used as a reference in order to convert the subject's positions from the POLARIS coordinate to the PET coordinate. Figure 1e shows an example of the experimental setup with a healthy volunteer in the cardiac PET study. Two targets were attached to the chest skin of the subject. Three legs of the supporting post were attached to the skin of the subject using surgical tape. The axial field-of-view (FOV) of the PET scanner used in the human study, HEADTOME-V tomography (SHIMADZU Corp., Kyoto, Japan), was 200 mm, and the gantry diameter was 850 mm [21]. The geometries of targets attached to the thoracic surface were 85×85 mm^2 (the left-hand target in Fig. 1e, target 1) and 65×90 mm^2 (the right-hand target in the Fig. 1e). The heights of supporting posts for target 1 and target 2 were 50 and 42 mm, respectively. We calculated the subject's positions in the PET coordinate by measuring the locations of the target with four infrared-reflective markers (the primary target). Another target was used as a reserve in cases when the primary target was hidden from the FOV of the POLARIS.

Motion correction

The rigid motion correction technique employed is an extension of the previous work for brain PET studies by

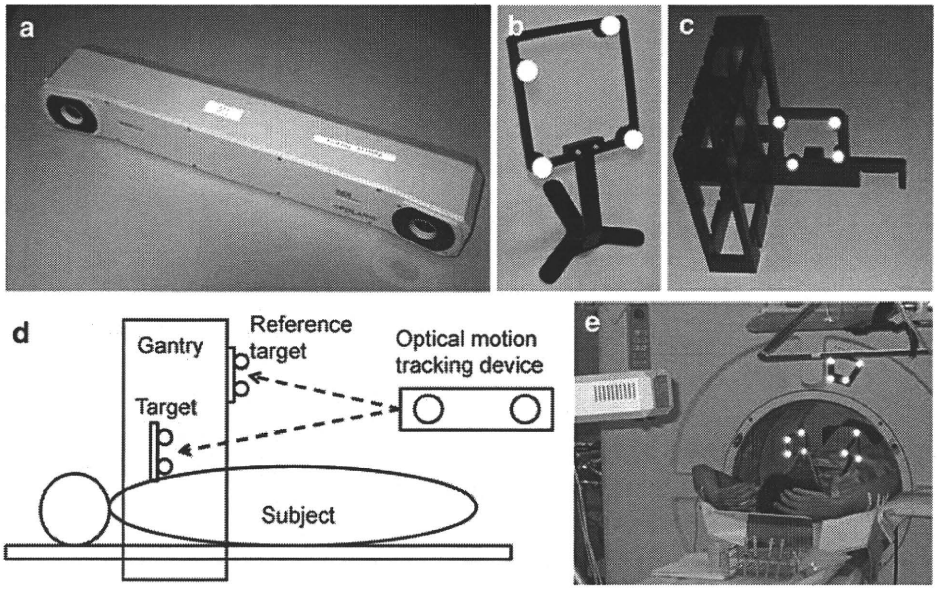

Fig. 1 Our motion correction system. **a** Optical motion-tracking device. **b** Target consists of infrared-reflective markers with supporting post. **c** Position calibration tool with a target. **d** Schematic diagram of the system. Locations of the targets on the subject and the gantry were measured with the optical motion-tracking device. **e** An example of the experimental configuration

Watabe et al. [4]. We consider four coordinates: the POLARIS C_S, a target on a PET gantry for reference C_G, a target attached on a subject C_T, and the PET scanner C_P. By measuring the location and orientation of each target attached to the subject and the gantry using the POLARIS, we obtained a 4 × 4 transformation matrixes, $T_{T\to S}$ from C_T to C_S, and $T_{G\to S}$ from C_G to C_S, respectively. Motion matrix $M_{P_1\to P_2}$ from a position $P_1 = P(t_1)$ to another position $P_2 = P(t_2)$ in the PET coordinate is written as follows [4]:

$$M_{P_1\to P_2} = T_{G\to P}T^{-1}_{G\to S}T_{T_1\to S}T^{-1}_{T_2\to S}T_{G\to S}T^{-1}_{G\to P} \quad (1)$$

where T_1 and T_2 are positions in target coordinates corresponding to positions P_1 and P_2 in the PET coordinate. $T_{G\to P}$ is the matrix to transform a position from the gantry coordinate to the PET coordinate. The matrix is given by the following equation:

$$T_{G\to P} = T_{S\to P}T_{G\to S} \quad (2)$$

$T_{S\to P}$ is the matrix which relates the POLARIS and PET coordinates and is obtained by position calibration.

The point source was embedded in a given position of a target, which is fixed on the calibration tool shown in Fig. 1c. By measuring the position of the point source using the POLARIS, the position $P_S = (x_S, y_S, z_S)$ of the point source in the POLARIS coordinate is calculated using the known position $P_T = (x_T, y_T, z_T)$ in the target coordinate and $T_{T\to S}$, as $P_S = T_{T\to S}P_T$. The position $P_P = (x_P, y_P, z_P)$ in the PET coordinate is also obtained from the reconstructed emission image. By changing the position of the target, in which the point source is embedded, $T_{S\to P}$ is calculated using the least-squared-fit between the pairs of P_Ss and P_Ps. The PET coordinate was

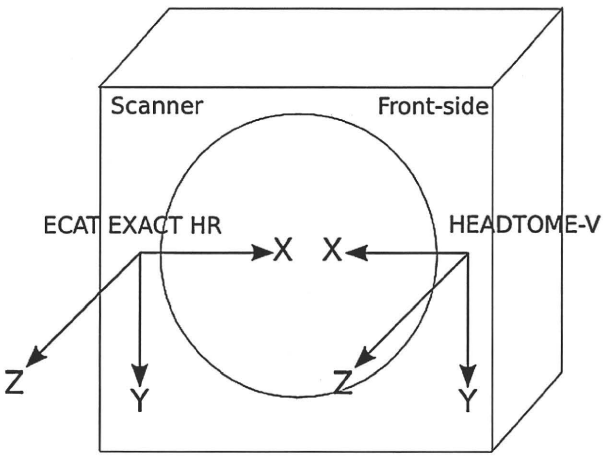

Fig. 2 PET coordinates defined by position calibrations

defined by the position calibration as shown in Fig. 2. The positions of subjects in the PET coordinate will be discussed in the following.

To correct a subject's movements during a dynamic acquisition of an emission scan with multiple frames, we estimated the heart locations from the locations of the target, which are measured by the POLARIS. The displacement of the COG of the heart's position from during the transmission scan to during each dynamic frame of the emission scan is given by

$$\begin{aligned} H^F - H^{TCT} &= \frac{1}{L}\sum_t^F H(t) - \frac{1}{N}\sum_t^{TCT} H(t) \\ &= \frac{1}{L}\sum_t^F [P(t) + \Delta(t)] - \frac{1}{N}\sum_t^{TCT} [P(t) + \Delta(t)] \end{aligned} \quad (3)$$

where H^{TCT} and H^{F} are the averaged COGs of the heart positions during the transmission and the dynamic frame, $H(t)$ and $P(t)$ are the COGs of positions of the heart and the target at time t, $\Delta(t)$ is a term representing a non-rigid relation for positions at time t between the heart and the target, L and N are the numbers of measurements of the target's positions by the POLARIS during acquisition of the dynamic frame and the transmission scan, respectively. For motion correction, we assumed the rigid body model, in which the target and the COG of the heart's position have linear movement at least in the FOV of a PET scanner, that is, we assumed that summations of $\Delta(t)$ for the transmission scan and the dynamic frame equal to zero. The procedures of our motion-correction technique are as follows: (1) An attenuation map is aligned to the coordinate of a dynamic frame of an emission scan using the motion matrix in Eq. 1, in which P_1 and P_2 are $\Sigma^{TCT}P(t)/N$ and $\Sigma^{F}P(t)/L$ in Eq. 3. (2) The attenuation map is then converted to its sinogram by forward projection. (3) Each sinogram of the dynamic frames is reconstructed with the realigned attenuation sinogram. (4) The emission image is aligned to the transmission coordinate with the inverse matrix of the motion matrix. (5) Last, procedures from 1 through 4 are repeated for all dynamic frames of the emission data.

Position calibrations

Position calibrations were performed on two PET scanners to obtain a matrix $T_{G\to P}$ in Eq. 2, which transforms the subject's positions from a gantry coordinate to a PET coordinate. For ECAT EXACT HR tomography (CTI/Siemens, Knoxville, TN, USA) [22] used in a cardiac phantom study, ten emission scans were performed, each displaying different positions of a radioactivity point source of ^{18}F solution, using the calibration tool in Fig. 1b. For the PET scanner used in a healthy volunteer study, 14 emission scans were performed with the ^{18}F solution point source and calibration tool.

The accuracy of the calibrations was evaluated from $T_{G\to S}$ and $T_{S\to P}$ in Eq. 2. The accuracy of $T_{G\to S}$ part was evaluated by determining the standard deviation (SD) of rotational angles and translations calculated from position data of the gantry, because $T_{G\to S}$ depends on only the accuracy of the measurements in regard to the POLARIS. To evaluate the accuracy of $T_{S\to P}$ part, we calculated errors between a position of a point source P_P, and the approximation position using $T_{S\to P}$, $P_X = T_{S\to P}P_S$:

$$e(i,k) = P_X(i,k) - P_P(i,k) \tag{4}$$

$$\mathrm{RMSE}(i) = \sqrt{\sum_{k=x,y,z} |P_X(i,k) - P_P(i,k)|^2} \quad (k = X,Y,Z \text{ and } i = 1,\ldots,N) \tag{5}$$

where $e(i, k)$ is the approximation error of a point source in the ith position for each direction, X, Y, and Z are orthogonal axes in Fig. 2, RMSE(i) is the root mean square error, and N is the number of positions of a point source.

Phantom study

To validate our correction technique for the misregistration between the attenuation map and emission data, we performed PET scans using a cardiac phantom (KYOTO KAGAKU co., LTD, Kyoto, Japan, type HL-D) and the ECAT EXACT HR tomography. The phantom mimics the human thoracic region and has cardiac and liver inserts. The insert can be filled with radioisotope solution. The myocardium and liver inserts were filled with the ^{18}F solution of relative activities of 1 and 4. A target (without the supporting port) for the POLARIS was attached to the phantom using polyethylene cross tape. Then, we performed a 1,000-s transmission scan for attenuation corrections. After the transmission scan, seven ^{18}F emission scans were performed with a set of single frame data for 180 s. The first scan was the baseline (scan #1), in which there was no misalignment to the transmission. For the following three emission scans (scan #2–4), the phantom was moved in the X, Y, and Z directions. For the other three scans, the phantom was rotated about the X, Y, and Z axes (scan #5–7). The phantom's positions were measured with the POLARIS.

The reconstructed images before and after the correction were obtained using an FBP (filtered back-projection) algorithm with a Gaussian filter of 6 mm FWHM (full-width at half-maximum). The matrix size and voxel size of images were 128 × 128 × 47 and 4.4 × 4.4 × 3.1 mm^3, respectively. All emission data were corrected for physical decay of ^{18}F with base time as the start of the first emission scan, and all of the emission images were reoriented to the short axis using a transformation matrix.

To evaluate the effects of the corrections, we calculated correlation coefficients for myocardial regions between the baseline and misaligned emission images, both before and after the corrections.

Human study

A cardiac ^{15}O-water PET study was performed on a healthy volunteer (male, 32 years old) using the HEADTOME-V tomography in order to validate use of the external markers on the chest skin and also to evaluate the effects of the global movement on the quantification of MBF by artificial misalignment between attenuation and emission data. The healthy volunteer gave written informed consent according to a protocol approved by the Ethical Committee and

Internal Review Board of Osaka University. The PET study consisted of a 20-min transmission scan, an 8-min ^{15}O-CO emission scan for blood pool imaging, a 6-min ^{15}O-water emission scan with 26 dynamic frames (12 × 5, 8 × 15 and 6 × 30 s), and a second 20-min transmission scan. All scans were acquired in a 2D acquisition mode. The radioactivity of inhaled ^{15}O-CO gas was 3.2 GBq. ^{15}O-water was injected via the left brachial vein; activity was 1.1 GBq for 40 s. All scans were performed without pharmacological stress. To investigate the accuracy of the POLARIS for tracking the locations of the target attached to the thorax skin of the subject, the couch of the PET scanner was moved +30 mm along the axial direction before the second transmission scan, corresponding to the Z direction in Fig. 2, with the subject lying on the couch. It was expected that the shift in the $+Z$ direction caused the artificial deterioration of image quality and quantitative accuracy in especially the anterior and lateral regions. The subject's positions during the scans were monitored by the POLARIS, at a frequency of one sample per second.

The reconstructed images for the four cases were obtained using an FBP algorithm with a Gaussian filter of 9 mm FWHM. The matrix and voxel sizes of the reconstructed images were 128 × 128 × 63 and 2.03 × 2.03 × 3.13 mm^3. No scatter correction was performed during the image reconstruction stage.

Regional MBF values were estimated for four cases. Case 1: the first attenuation map and emission data, case 2: the first attenuation map and emission data with correction for the subject's motions, case 3: the second attenuation map and the emission data, case 4: the second attenuation map and the emission data after the correction for the subject's motions and the 30-mm-shifted misalignment. Differences in the MBF values for cases 1 and 2 were considered to indicate effects from the correction for the frame-averaged motion if the subject's motion was small. Differences in MBF values for cases 1 and 3 could indicate errors in the quantification of MBF caused by the artificial misalignment between the second attenuation map and the emission data. The lack of any difference in MBF values for cases 1 and 4 indicated that our technique tracked the shift of the target on the thorax skin accurately and corrected the misalignment. In order to generate cases 2 and 4, the positions P_1 and $P_2^{(j)}$ in Eq. 1 were calculated as averaged COGs of the subject's positions during the first and second transmission scans and the jth dynamic frame of ^{15}O-water or C^{15}O emission scan. Using Eq. 1 with P_1 and $\{P_2^{(j)}\}$, we performed frame-by-frame motion corrections for all dynamic frames of emission data. Due to the fact that the PET scanner did not provide a dynamic transmission scan, we assumed that the subject did not move during the transmission scan.

For quantification of MBF, we employed a compartment analysis model proposed by Iida et al. [13], which provided corrections for spillover from a left ventricle and partial volume effect and generated a MBF value in units of mL/min/g of perfusable tissue. All transmission and emission images were reoriented to the short axis. To calculate tissue time activity curves, regions of interest (ROIs) were drawn in nine myocardial regions: apical, mid-anterior, mid-lateral, mid-posterior, mid-septal, basal-anterior, basal-lateral, basal-posterior, and basal-septal regions. To avoid spillover effects from the right ventricle, the sizes of ROIs in septal regions were smaller than those in other regions. Another ROI was drawn on the left ventricle in order to estimate the arterial input function [19]. These ROIs were manually and independently drawn for the four cases. In addition, to validate the consistency between the quantitative results of MBF values and the quality of the images, we calculated the build-up and washout phase images [23] for the four cases. The build-up and washout phase images were obtained by subtracting a blood pool image from summed images of early (0–180 s) and later (180–360 s) frames of a ^{15}O-water image.

We evaluated the magnitude of the subject's motions in the PET coordinate during each scan. We defined position P_1 in Eq. 1 as the position at the start of the first transmission scan, and position P_2 as the position at an arbitrary time during a transmission or an emission scans. The rotational angles and translations for arbitrary times were obtained using Eq. 1. We represented motion during a scan in the form of mean ± SD for each rotational angle and translation.

Results

Position calibrations

Table 1 shows the inherent accuracy of our system in the two PET scanners. Values of SDs for rotations and translations obtained from $T_{G\to S}$ data were very small. Table 1 also shows the approximation errors (mean ± SD) occurred while transforming the positions of a point source from the POLARIS coordinate to the PET coordinate using $T_{S\to P}$. There was no bias in any direction in either scanner. Each value of RMSE was smaller than the spatial resolution of the corresponding scanner [21, 22].

Cardiac phantom study

Table 2 lists the observed misalignment from the reference position of the phantom in the transmission scan and the correlation coefficients between the reference image and the misaligned images before and after the corrections (mean ± SD; 0.929 ± 0.022 and 0.987 ± 0.010). The

Table 1 Inherent accuracy of the motion correction system in the two PET scanners

Scanner	$T_{G\to S}$						$T_{S\to P}$				# of point positions
	Rotational angle (deg)			Translation (mm)			e_x	e_y	e_z	RMSE	
	r_x	r_y	r_z	t_x	t_y	t_z					
ECAT EXACT HR	0.0	0.0	0.0	0.0	0.0	0.0	0.0 ± 0.8	0.0 ± 0.9	0.0 ± 0.8	1.3 ± 0.4	10
HEADTOME-V	0.0	0.0	0.0	0.0	0.0	0.1	0.0 ± 1.5	0.0 ± 1.6	0.0 ± 0.6	2.3 ± 0.2	14

Standard deviations of rotational angles and translations obtained from $T_{G\to S}$ data and approximation errors (mean ± SD in mm) by transforming positions of a point source from the POLARIS coordinate to the PET coordinate using $T_{S\to P}$. Columns $T_{G\to S}$, r_x, r_y and r_z denote SDs of rotational angles about three orthogonal X, Y, and Z axes, respectively. t_x, t_y and t_z denote SDs of translations along three orthogonal axes, respectively. Columns $T_{S\to P}$, e_x, e_y, and e_z denote average values (mean ± SD in mm) of $e(i, X)$, $e(i, Y)$, and $e(i, Z)$, respectively. $e(i, k)$ was defined in Eq. 4. *RMSE* denotes an average value (mean ± SD in mm) of *RMSE*(i), defined in Eq. 5

Table 2 The observed misalignment and correlation coefficients for the phantom study

Scan no.	Rotation (deg)			Translation (mm)			Correlation coefficient	
	r_x	r_y	r_z	t_x	t_y	t_z	Before MC	After MC
2	0.0	0.2	5.1	35.7	0.8	−3.4	0.896	0.997
3	0.0	−1.0	1.3	0.9	35.2	3.2	0.938	0.995
4	0.0	−0.2	0.9	5.9	0.1	42.8	0.917	0.971
5	13.1	1.4	0.4	1.9	22.5	17.1	0.926	0.986
6	2.4	−15.6	−2.1	10.9	3.8	4.7	0.938	0.982
7	−0.6	1.8	−13.5	13.4	11.9	−9.5	0.960	0.992

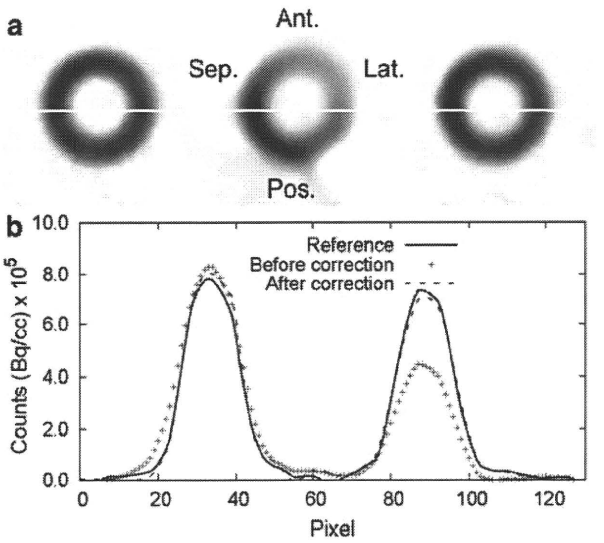

Fig. 3 Reconstructed and reoriented images of the phantom. **a** Reconstructed images. *Left*, *mid*, and *right* columns represent the reference emission image (no misalignment), the second emission images before correction for misalignment, and the second emission images after correction for the misalignment, respectively. **b** Profiles at the level of white lines in images. *Solid line*, *cross symbols*, and *dashed lines* represent the first emission image, the second emission images before correction, and the second emission images after correction, respectively

effects of our correction technique are demonstrated in Fig. 3. The left column in Fig. 3a is the reference emission image (no misalignment). The middle and right columns represent the emission images with the misalignment of the X-direction before and after the corrections. For the image in the middle column, only the position was transformed to the transmission coordinate after the reconstruction. Figure 3b represents line profiles at the level of white lines in the slices.

Human study

Table 3 summarizes the observed movements of the subject during scans relative to the beginning of the first transmission scan, in the form of rotational angles about and translations along three orthogonal axes. It was observed that the magnitude of the average parts of the rotational angles and translations tended to increase. The value of t_z changed from −1.8 ± 0.6 to 28.3 ± 0.6 mm between the ^{15}O-water emission and the second transmission scan mainly because of the 30-mm shift of the couch as well as the motions of the subject. There was little change in the SD in any rotational angle or translation among the scans.

Figure 4 shows motion parameters during ^{15}O-water scan. Figure 4a and b represent the sample-by-sample and frame-averaged translations. Figure 4c and d shows the sample-by-sample and frame-averaged rotational angles.

Table 4 shows that the MBF values (mean ± SD), which were obtained from nine myocardial segments, were 0.94 ± 0.12, 0.91 ± 0.13, 1.03 ± 0.21, and 0.93 ± 0.11 mL/min/g for the four cases. The values for cases 1 and 2 were obtained from the emission data and the first attenuation map before and after motion correction. The values for cases 3 and 4 were obtained from the emission data and the second attenuation map before and after the corrections for the subject's motions and the 30-mm shift of the couch. There were significant

Table 3 Observed movements (mean ± SD) of the healthy volunteer during scans relative to the beginning of the first transmission scan

Scan	Rotational angle (deg)			Translation (mm)		
	r_x	r_y	r_z	t_x	t_y	t_z
TCT 1	−0.1 ± 0.2	−0.4 ± 0.2	−0.2 ± 0.2	0.7 ± 0.5	1.3 ± 0.6	1.0 ± 0.8
$C^{15}O$	0.0 ± 0.2	−0.1 ± 0.2	−0.7 ± 0.1	2.6 ± 0.3	1.0 ± 0.5	−1.7 ± 0.7
^{15}O-water	0.4 ± 0.2	0.0 ± 0.1	−0.7 ± 0.1	2.7 ± 0.2	1.3 ± 0.4	−1.8 ± 0.6
TCT 2	−0.4 ± 0.2	0.7 ± 0.2	−2.0 ± 0.1	3.7 ± 0.3	2.6 ± 0.5	28.3 ± 0.6

r_x, r_y, and r_z denote rotational angles (degrees) about X, Y, and Z-axes, respectively. t_x, t_y, and t_z denote translations (mm) along *X*, *Y*, and *Z* axes, respectively

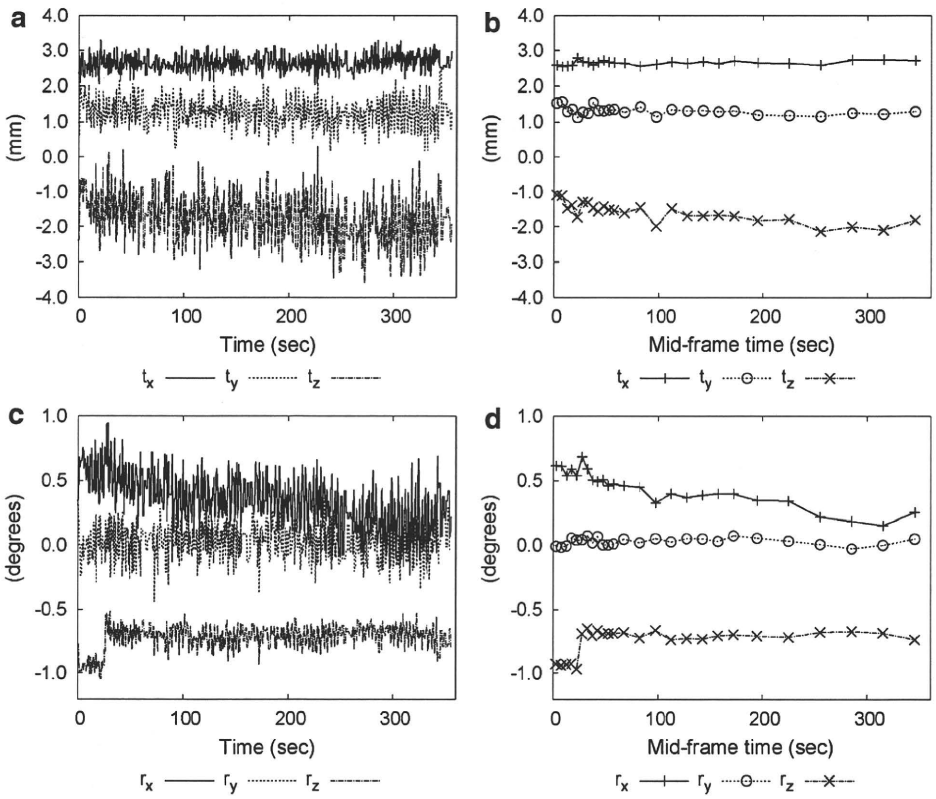

Fig. 4 Motion parameters during ^{15}O-water study on the healthy volunteer. **a**, **b** Sample-by-sample and frame-averaged translations. **c**, **d** Sample-by-sample and frame-averaged rotational angles

Table 4 MBF values (mL/min/g of perfusable tissue) of the healthy volunteer

Myocardial region	Case			
	1	2	3	4
Apical	1.05	1.00	0.99	1.05
Mid-anterior	0.92	0.89	1.26	0.99
Mid-lateral	0.93	0.89	1.38	0.89
Mid-posterior	1.14	1.16	0.96	1.01
Mid-septal	1.05	1.06	1.08	1.12
Basal-anterior	0.87	0.80	1.18	0.80
Basal-lateral	0.86	0.82	0.95	0.84
Basal-posterior	0.88	0.83	0.84	0.86
Basal-septal	0.73	0.72	0.65	0.82
Mean ± SD	0.94 ± 0.12	0.91 ± 0.13	1.03 ± 0.21	0.93 ± 0.11

differences in the mid-anterior and mid-lateral regions as well as the basal-anterior regions between cases 1 and 3.

Figure 5 demonstrates the influence of misalignment between an attenuation map and emission data on the quality of myocardial images, as well as the effect of our correction technique. Figure 5a–f represent the build-up and washout phase images of middle myocardial obtained from the ^{15}O-water data. Anterior, lateral, posterior, and septal regions of myocardia were arranged in a clockwise manner. Figure 5a and e was obtained from the data of case 1, and Fig. 5b and f was calculated from the data obtained in case 2. Figure 5c and g was derived from the data in case 3, and only positions of reconstructed images were transformed to the first transmission coordinate after reconstructions for visual

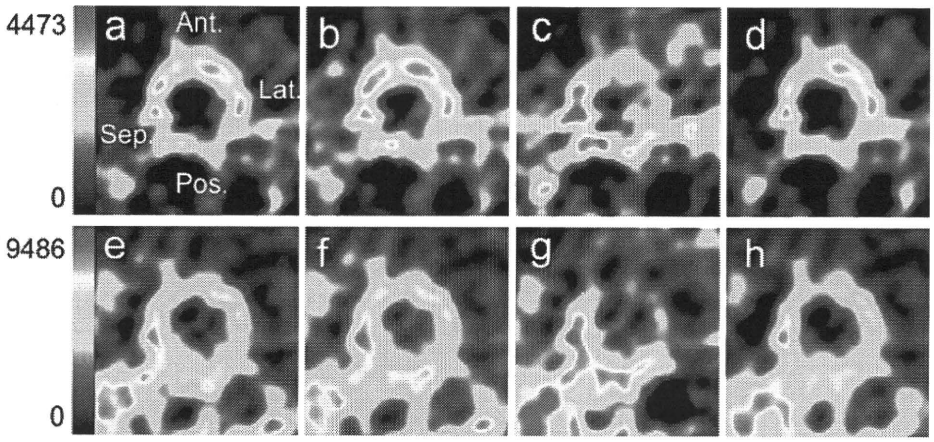

Fig. 5 Myocardial images of the healthy volunteer. **a–d** Build-up phase images. **e–h** Washout phase images. **a** and **e** were reference images obtained from data of case 1. **b** and **f** are images from data of case 2, which were corrected for the motions of the subject. **c** and **g** are images from case 3 of the emission data and the second attenuation map without our motion corrections. **d** and **h** are images from case 4, which were corrected for the motions and the misalignment between the emission data and the second attenuation map

comparison with the other images. Figure 5c and g demonstrates that reconstruction with an incorrect attenuation map caused spurious defects from anterior to lateral myocardial regions, as well as an artifact in the posterior region. Figure 5d and h is an image calculated from data obtained in case 4, in which images were also transformed to the first transmission coordinate.

Discussion

In this paper, we developed an optical motion-tracking based system to detect global movement of the subject and correct for the movement during cardiac ^{15}O-water studies.

First, the inherent accuracy of the system was assessed from position calibrations. As shown in Table 1, the $T_{G\rightarrow S}$ part could be negligibly small compared with the magnitude of the subject's motions in Table 3 and Fig. 4. For the $T_{S\rightarrow P}$ part shown in Table 1, there was no bias in any direction. The value of RMSE for each scanner was smaller than the spatial resolution of the scanner [21, 22]. Therefore, it was considered that the position calibrations provided a sufficient level of accuracy for our motion corrections.

To validate the present technique, we performed a cardiac phantom study. As shown in Fig. 3a, a defect and blurred region from the anterior to the lateral, which was mainly caused by a 5.1° rotation about the Z axis and a 35.7 mm shift along the X axis, was recovered using the present technique. The effect of the present technique was also shown more objectively by the correlation coefficients and profile comparison in Fig. 3b.

In the healthy volunteer study, no correction was applied for the motions of the subjects during the transmission scans because the PET scanners do not have the ability to perform dynamic transmission scans. Motions during a transmission scan resulted in a blurred attenuation map, and caused over- or under-estimation of the radioactive concentration in myocardium of ^{15}O-water images. However, as shown in Table 3, the magnitudes of the mean and SD during the transmission scans were smaller than the spatial resolution provided by the PET scanner, even if the magnitudes were slightly larger than those of the mean and SD during emission scans. In addition, a 9-mm smoothing filter was employed during the image reconstruction stage. Therefore, we considered that valid transmission data were acquired for the subject. For the same reason as in the case of the transmission data, the emission data of ^{15}O-water scan were acquired properly. So we used the data of case 1 as the reference for the other cases.

The global movement and cyclic movement of the target were observed as shown in Fig. 4a and c. The cyclic movement was attributed to respiration. From Fig. 4b and d, the cyclic movement was smoothed by frame-averaging. In addition, the regional MBF values (Table 4) and the myocardial images (Fig. 5) of cases 1 and 2, which were derived from the same transmission and emission scans before and after the motion correction, were nearly the same. This result indicated that our system provided reasonably accurate information about the global movement.

In case 3, in which no correction for the subject's motions and the 30-mm shift between the emission data and the second attenuation map was applied, the MBF values for the mid-anterior, mid-lateral, and basal-anterior regions were

significantly larger than the reference values. This overestimation was associated with spurious defects from the anterior to lateral regions, as shown in Fig. 5c and g. In case 4 with our correction technique, the MBF values for myocardial regions, in which overestimated MBFs were obtained for the corresponding regions in case 3, were similar to the reference values. The image quality in Fig. 5d and h was also nearly the same as in Fig. 5a and e. Figure 5d shows a clearly delineated contour of the myocardial region similar to the contour in Fig. 5a. The spurious defects from the anterior to lateral regions in Fig. 5g were recovered in Fig 5h. Owing to these results, the present technique tracked the location of the external target attached to the chest skin accurately, and then corrected the artificial misalignment during transmission and emission scans. Figure 5 not only shows the effects of our correction technique, but also suggests that the use of an attenuation map with large global movement could cause the appearance of spurious defects in myocardial imaging with ^{15}O-water PET.

Several listmode-based motion correction techniques have hitherto been proposed [1, 3–7]. Compared to these techniques, our technique provides poorer time resolution, even though our technique was applied to an emission scan consisting of dynamic frames with shorter duration. Listmode-based methods, however, require wide band transmission and high computational power for manipulating the listmode event data, especially under high count rates. For the listmode-based methods, in which data processing is conducted prior to the motion correction, corrections for detector efficiency, detector geometry, and crystal interferences are important issues, especially in the case of scanners with gaps between detectors or no intersection of motion-corrected LOR with detector(s). For our technique with 2D acquisition mode, the sinogram data are simply normalized by the built-in software of the used PET scanners. Our technique could shorten the processing time by re-binning the listmode data during the period when substantial movement is detected, and then correcting the re-framed dynamic sinogram. Furthermore, our technique is applicable to many commercially available PET scanners, which often have no feasibility of listmode acquisition.

Instead fixating the POLARIS on a certain position, such as the gantry of the PET scanner described in [3, 6], we attached the reference target onto the gantry and then used the target and the calibration tool to transform the subject's position from the POLARIS coordinate to the PET coordinate. Thus, our method allows for more flexibility in adjusting with regard to the location of the POLARIS. This is an important feature for the cardiac study due to the large inter-subject variability in the shapes of the torsos among patients, and as shown in Fig. 1e, there were enough gaps to set the best positioning for cardiac PET study. However, for exercise study, such as the studies with cycling, smaller targets and supporting post might be needed to ensure working space. An additional advantage is the portability of the POLARIS, which enables the sharing of the device among scanners in different locations.

For our technique based on the rigid body model, two targets were enough to detect the displacements and rotations of the thoraxes of the subjects, in which the secondary target was used as a reserve for cases in which the primary target was hidden from the FOV of the POLARIS. The secondary target and additional targets might be used with the corporation of the primary target to construct a non-rigid body model by detecting deformation between the chest and abdomen, and/or over the thorax region.

Another approach for the motion correction was based on image-driven information. Juslin et al. proposed an alignment technique for dynamic ^{15}O-water PET images by means of the independent component analysis. They demonstrated an improvement in quantitatively functional and parametric values, although they did not take into account for the misregistration between the transmission and emission data sets, and the movements during each emission scan [24]. The advantages of our method comparing software-based technique were (1) the misalignment between the transmission and dynamic image, and misalignment among the dynamic images could be corrected because our method was independent of the distribution and concentration of the tracer, and suboptimal image qualities (e.g., statistical noise, blurring and types of tracers). (2) Accurate attenuation correction was available because the misalignment between the transmission and the dynamic image was corrected in the reconstruction stage of the dynamic image, and (3) inherent accuracy could be obtained from the position calibration and the optical motion tracking device. Consequently, the present technique can be utilized in PET studies with several types of tracers such as ^{13}N-Ammonia and ^{18}F-FDG.

In this study, the motion correction system was demonstrated on one subject at rest. The system is to be evaluated by large population of various subjects because characteristics of motion such as magnitudes, frequencies, and directions could be different among subjects. Validation of our system is also needed for the studies during the physiologically or pharmacologically stressed conditions, in which repositioning of the heart in thoracic cavity, and larger and/or irregular (non-cyclic) chest motion by respiration would be expected. In our method, one of the limitations was correction for the misalignment due to the motion of the diaphragm with a deep breathing during a stress study, and due to the motion of the diaphragm with cough or sneezing even though during a resting study. To correct such misalignment, detection of irregular motion and a non-linear model might be needed to estimate the

location of the heart using information obtained from the locations of targets on the chest.

Our system intended to correct global movement during dynamic scans. It was expected that the system would work on transmission and emission data smoothed temporally and spatially. Attenuation correction artefacts due to respiration was out of the scope for our system, which were investigated in the X-ray combined PET system studies [25, 26].

Conclusion

Our technique using an optical motion-tracking device provided the reasonable information for correcting the global movement of the subject. It was shown that this system was applicable to detect and correct subject movement in cardiac PET studies at rest. We conclude that the present technique would contribute to improvement in the quantification of MBF in ^{15}O-water PET studies.

Acknowledgments This study was supported by a grant from New Energy and Industrial Technology Development Organization (NEDO) of Japan, the Budget for Nuclear Research of the Ministry of Education, Culture, Sports, Science and Technology (MEXT) of Japan, the Program for Promotion of Fundamental Studies in Health Science of the Organization for Pharmaceutical Safety and Research of Japan, Health Science Research Grant from the Ministry of Health, Labour and Welfare of Japan, a Grant-in-Aid for Young Scientists of the MEXT (B) (19700397) of Japan, and also a research grant for Advanced Medical Technology from the Ministry of Health, Labour and Welfare (MHLW) of Japan.

References

1. Menke M, Atkins MS, Buckley KR. Compensation methods for head motion detected during PET imaging. IEEE Trans Nucl Sci. 1996;43:310–7.
2. Picard Y, Thompson CJ. Motion correction of PET images using multiple acquisition frames. IEEE Trans Med Imaging. 1997;16:137–44.
3. Lopresti BJ, Russo A, Jones WF, Fisher T, Crouch D, Altenburger DE, et al. Implementation and performance of an optical motion tracking system for high resolution brain PET imaging. IEEE Trans Nucl Sci. 1999;46:2059–67.
4. Watabe H, Sato N, Kondoh Y, Fulton RR, Iida H. Correction of head movement using optical motion tracking system during PET study with rhesus monkey. In: Brain Imaging Using PET. San Diego: Academic Press; 2002. p. 1–8.
5. Fulton RR, Meikle SR, Eberl S, Pfeiffer J, Constable CJ. Correction for head movements in positron emission tomography using an optical motion-tracking system. IEEE Trans Nucl Sci. 2002;49:116–23.
6. Bloomfield PM, Spinks TJ, Reed J, Schnorr L, Westrip AM, Livieratos L, et al. The design and implementation of a motion correction scheme for neurological PET. Phys Med Biol. 2003;48:959–78.
7. Woo SK, Watabe H, Yong C, Kim KM, Choon C, Bloomfield PM, et al. Sinogram-based motion correction of PET images using optical motion tracking system and list-mode data acquisition. IEEE Trans Nucl Sci. 2004;51:782–8.
8. McCord ME, Bacharach SL, Bonow RO, Dilsizian V, Cuocolo A, Freedman N. Misalignment between PET transmission and emission scans: its effect on myocardial imaging. J Nucl Med. 1992;33:1209–14.
9. Germano G, Chua T, Kavanagh PB, Kiat H, Berman DS. Detection and correction of patient motion in dynamic and static myocardial SPECT using a multi-detector camera. J Nucl Med. 1993;34:1349–55.
10. Cooper JA, Neumann PH, McCandless BK. Detection of patient motion during tomographic myocardial perfusion imaging. J Nucl Med. 1993;34:1341–8.
11. Bacharach SL, Douglas MA, Carson RE, Kalkowski PJ, Freedman NM, Perrone-Filardi P, et al. Three-dimensional registration of cardiac positron emission tomography attenuation scans. J Nucl Med. 1993;34:311–21.
12. Iida H, Kanno I, Takahashi A, Miura S, Murakami M, Takahashi K, et al. Measurement of absolute myocardial blood flow with $H_2^{15}O$ and dynamic positron-emission tomography. Strategy for quantification in relation to the partial-volume effect. Circulation 1988;78:104–15 (erratum in: Circulation 1988;78:1078).
13. Iida H, Rhodes CG, de Silva R, Yamamoto Y, Araujo LI, Maseri A, et al. Myocardial tissue fraction–correction for partial volume effects and measure of tissue viability. J Nucl Med. 1991;32:2169–75.
14. Knaapen P, Boellaard R, Götte MJ, van der Weerdt AP, Visser CA, Lammertsma AA, et al. The perfusable tissue index: a marker of myocardial viability. J Nucl Cardiol. 2003;10:684–91.
15. de Silva R, Yamamoto Y, Rhodes CG, Iida H, Nihoyannopoulos P, Davies GJ, et al. Preoperative prediction of the outcome of coronary revascularization using positron emission tomography. Circulation. 1992;86:1738–42.
16. Knaapen P, Boellaard R, Götte MJ, Dijkmans PA, van Campen LM, de Cock CC, et al. Perfusable tissue index as a potential marker of fibrosis in patients with idiopathic dilated cardiomyopathy. J Nucl Med. 2004;45:1299–304.
17. Chareonthaitawee P, Kaufmann PA, Rimoldi O, Camici PG. Heterogeneity of resting and hyperemic myocardial blood flow in healthy humans. Cardiovasc Res. 2001;50:151–61.
18. Yamamoto Y, de Silva R, Rhodes CG, Araujo LI, Iida H, Rechavia E, et al. A new strategy for the assessment of viable myocardium and regional myocardial blood flow using 15O-water and dynamic positron emission tomography. Circulation. 1992;86:167–78.
19. Iida H, Rhodes CG, de Silva R, Araujo LI, Bloomfield PM, Lammertsma AA, et al. Use of the left ventricular time-activity curve as a noninvasive input function in dynamic oxygen-15-water positron emission tomography. J Nucl Med. 1992;33:1669–77.
20. Naum A, Laaksonen MS, Tuunanen H, Oikonen V, Teräs M, Kemppainen J, et al. Motion detection and correction for dynamic (15)O-water myocardial perfusion PET studies. Eur J Nucl Med Mol Imaging. 2005;32:1378–83.
21. Iida H, Miura S, Kanno I, Ogawa T, Uemura K. A new PET camera for noninvasive quantitation of physiological functional parametric images: HEADTOME-V-Dual. In: Quantification of brain function using PET. San Diego: Academic Press; 1996. 57–61.
22. Wienhard K, Dahlbom M, Eriksson L, Michel C, Bruckbauer T, Pietrzyk U, et al. The ECAT EXACT HR: performance of a new high resolution positron scanner. J Comput Assist Tomogr. 1994;18:110–8.

23. Iida H, Rhodes CG, Araujo LI, Yamamoto Y, de Silva R, Maseri A, et al. Noninvasive quantification of regional myocardial metabolic rate for oxygen by use of $^{15}O_2$ inhalation and positron emission tomography. Theory, error analysis, and application in humans. Circulation. 1996;94:792–807.
24. Juslin A, Lötjönen J, Nesterov SV, Kalliokoski K, Knuuti J, Ruotsalainen U. Alignment of 3-dimensional cardiac structures in O-15-labeled water PET emission images with mutual information. J Nucl Cardiol. 2007;1:82–91.
25. McQuaid SJ, Hutton BF. Sources of attenuation-correction artefacts in cardiac PET/CT and SPECT/CT. Eur J Nucl Med Mol Imaging. 2008;35:1117–23.
26. Gould KL, Pan T, Loghin C, Johnson NP, Guha A, Sdringola S. Frequent diagnostic errors in cardiac PET/CT due to misregistration of CT attenuation and emission PET images: a definitive analysis of causes, consequences, and corrections. J Nucl Med. 2007;48:1112–21.

Impaired Myocardium Regeneration With Skeletal Cell Sheets—A Preclinical Trial for Tissue-Engineered Regeneration Therapy

Shigeru Miyagawa,[1] Atsuhiro Saito,[2] Taichi Sakaguchi,[1] Yasushi Yoshikawa,[1] Takashi Yamauchi,[1] Yukiko Imanishi,[1] Naomasa Kawaguchi,[3] Noboru Teramoto,[4] Nariaki Matsuura,[3] Hidehiro Iida,[4] Tatsuya Shimizu,[5] Teruo Okano,[5] and Yoshiki Sawa,[1,6]

Background. We hypothesized that autologous skeletal cell (SC) sheets regenerate the infract myocardium in porcine heart as a preclinical trial.

Methods and Results. The impaired heart was created by implantation of ameroid constrictor on left anterior descending for 4 weeks. SCs isolated from leg muscle were cultured and detached from the temperature-responsive domain-coated dishes as single monolayer cell sheet at 20°C. The following therapies were conducted: SC sheets (SC group, n=5); sham (C group n=5). Echocardiography demonstrated that cardiac performance was significantly improved in the SC group 3 and 6 months after operation (fractional area shortening, 3 months; SC vs. C=49.5±2.8 vs. 24.6±2.0%, $P<0.05$) and left ventricle dilatation was well attenuated in the SC group. Color kinesis index showed that distressed regional diastolic and systolic function in infarcted anterior wall was significantly recovered (SC vs. C=57.4±8.6 vs. 30.2±4.7%, $P<0.05$, diastolic: 58.5±4.5 vs. 35.4±6.6%, $P<0.05$, systolic). Factor VIII immunostains demonstrated that vascular density was significantly higher in the SC group than the C group. And % fibrosis and cell diameter were significantly lower in the SC group. And hematoxylin-eosin staining depicted that skeletal origin cells and well-developed-layered smooth muscle cells were detected in the implanted area. Positron emission tomography showed better myocardial perfusion and more viable myocardial tissue in the distressed myocardium receiving SC sheets compared with the myocardium receiving no sheets.

Conclusions. SC sheet implantation improved cardiac function by attenuating the cardiac remodeling in the porcine ischemic myocardium, suggesting a promising strategy for myocardial regeneration therapy in the impaired myocardium.

Keywords: Cells, Heart failure, Myocardial infarction, Tissue, Transplantation.

(*Transplantation* 2010;XX: 000–000)

Despite the recent remarkable progress in medical and surgical treatments for heart failure, end-stage heart failure has been still a major cause of death worldwide. After myocardial infarction, the myocardium is capable of a limited regenerative capacity and no medication or procedure used clinically has shown efficacy in regenerating myocardial scar tissue with functioning tissue. Thus, there is a need for new therapeutics to regenerate damaged myocardium.

Recent developments in tissue engineering show promise for the creation of functional cardiac tissues without the need for biodegradable alternatives for the extracellular matrix (*1*). And we reported that cardiomyocyte sheets have been developed by using temperature-responsive culture dishes and these sheets survived in the back of nude rats and showed a spontaneous contraction over a long period of time (*2*). Recent reports suggested that cardiomyocyte sheets integrated with the impaired myocardium and improved cardiac performance in a rat model of ischemic myocardium (*3*).

This work was supported by a Grant-in-Aid for Scientific Research in Japan.

[1] Division of Cardiovascular Surgery, Department of Surgery, Faculty of Medicine, Osaka University Graduate School of Medicine, Suita, Osaka, Japan.

[2] Medical Center for Translational Research, Osaka University Hospital, Osaka, Japan.

[3] Department of Pathology, School of Allied Health Science, Faculty of Medicine, Osaka University Graduate School of Medicine, Suita, Osaka, Japan.

[4] Department of Investigative Radiology, National Cardiovascular Center Research Institute, Tokyo, Japan.

[5] Tokyo Women's Medical University Institute of Advanced Biomedical Engineering and Science, Tokyo, Japan.

[6] Address correspondence to: Yoshiki Sawa, M.D., Department of Cardiovascular Surgery, Osaka University Graduate School of Medicine, 2-2 Yamada-oka, Suita, Osaka 565-0871, Japan.
E-mail: sawa@surg1.med.osaka-u.ac.jp

S.M. participated in the writing of the paper; A.S. participated in research design; T.S. and Y.Y. participated in data analysis; T.Y., Y.I., N.K., and N.T. participated in the performance of research; N.M., H.I., T.S., T.O., and Y.S. participated in research design.

Received 27 February 2010. Revision requested 27 February 2010.
Accepted 15 March 2010.

ISSN 0041-1337/10/XX0X-1
DOI: 10.1097/TP.0b013e3181e6f201

And more recently, in the aim of clinical application, nonligature implantation of skeletal myoblast sheet regenerated the damaged myocardium and improved global cardiac function by attenuating the cardiac remodeling in the rat ligation model (*4*) and dilated cardiomyopathy hamster model (*5*). This cell delivery system by using cell sheets implantation showed better restoration of damaged myocardium compared with needle injection (*4*, *5*). Moreover, grafting of skeletal myoblast sheets attenuated cardiac remodeling and improved cardiac performance in pacing-induced canine heart failure model (*6*).

Given this body of evidence, we hypothesized that the autologous skeletal cell (SC) sheet implantation might remodel the chronic heart failure caused by ischemic injury.

Therefore, this preclinical study using Swine model was designed to test therapeutic effectiveness.

METHOD

Myocardial Infarction Model

"Principles of Laboratory Animal Care" formulated by the National Society for Medical Research and the "Guide for the Care and Use of Laboratory Animals" prepared by the Institute of Laboratory Animal Resource and published by the National Institutes of Health (NIH Publication No. 86-23, revised 1985). This animal experiment was approved by the Animal Care Committee of Osaka university graduate school of medicine. We induced acute myocardial infarction of 10 swine (20 kg, KEARI, Japan) by the following method. Swine were preanesthetized by intramuscular injection of ketamine hydrochloride 20 mg/kg (Ketalar, Sankyo, Japan) and xylazine 2 mg/kg (Seractar, Bayer). Animals were positioned spine and a 22-gauge indwelling needle (Surflo F&F, Terumo, Tokyo, Japan) was inserted in the central vein of the auricle. A three-way cock (Terufusion TS-TR2K, Terumo, Tokyo, Japan) was attached to the external cylinder of the indwelling needle, and an extension tube was connected for continuous anesthetic injection. The animals were intubated with an endotracheal cannula (6 Fr, Sheridan) using a pharyngoscope and then connected to an artificial respirator (Harvard, USA) by the cannula. Artificial respiration was implemented at a stroke volume of 200 to 300 mL/stroke and a stroke frequency of 20/min. The animals were continuously drip injected with propofol 6 mg/kg/hr (Diprivan, AstraZeneca) and vecuronium bromide 0.05 mg/kg/hr (Musculux, Sankyo Yell Yakuhin Co., Ltd., Japan) using a syringe pump (Terufusion TE-3310N, Terumo, Japan). The animal was then fixed in a recumbent position, so that the left thorax was exposed, and the outer layer of skin and muscles between the third and fourth ribs were dissected. After confirming the cutting into the thoracic cavity, the distance between the third and fourth ribs was widened with a rib spreader to allow a direct view of the left auricle and the LAD coronary artery. The pericardium was dissected along the LAD from the upper part of the left auricle (~6 cm) to expose the myocardium around the LAD. LAD on the proximal side below the left auricle from the myocardium was exfoliated for approximately 1 cm, and then a small amount of lidocaine hydrochloride jelly (Xylocaine jelly, AstraZeneca) was applied to allow for anesthetizing the area. An ameroid constrictor (COR-2.50-SS, Research Instruments) was then fit using No. 1 or 2 suture. The chest cavity was closed to end the procedures. The animals were randomly divided into two treatment groups: the first received autologous SC sheet implantation (SC group, n=5). For control, we have performed sham operation (C group, n=5).

Preparation of Skeletal Cell Sheets for Grafting

One week after implantation of ameroid constrictor on LAD, skeletal muscle weighing approximately 5 g was removed from the pretibial region with the porcine under general anesthesia. Following the addition of trypsin-ethylenediaminetetraacetic acid (Gibco, Grand Island, NY), excessive connective tissue was carefully removed to minimize the content of contaminating fibroblasts, and the muscle tissue was minced until the fine pieces formed a homogeneous mass. The specimens were then incubated at 37°C in shaker bath with 0.5% type 1 collagenase (Gibco) in Dulbecco's modified Eagle's medium (Gibco). After brief placement, the fluid was collected, and the same volume of culture medium, SkBM (Cambrex, Walkersville, MD) supplemented with fetal bovine serum (Thermo Trace, Melbourne, Australia), was added to halt the enzymatic digestion process. The cells were collected by centrifugation, and the putative SCs were seeded into 150 cm^2 polystyrene flasks after removal of fibroblasts by sedimentation for a few hours and cultured in SkBM at 37°C. During the culture process, we maintained cell densities at less than 70% confluence by carrying out passaging of cells for one time to prevent SCs from premature differentiation and fusion process resulting in myotubes formation. When the cells become approximately 70% confluent after 10 to 11 days cultivation, the cells were dissociated from the flasks with trypsin-ethylenediaminetetraacetic acid and reincubated on 100 mm temperature-responsive culture dishes (Cellseed, Tokyo, Japan) at 37°C with the cell numbers adjusted to 1×10^7 per dish. More than 90% of these cells were desmin positive (Fig. 1). After 4 days, the dishes were removed to refrigerator set at 20°C, and left there for approximately 30 min. During that time, the SC sheets detached spontaneously from the surfaces. Each sheet had a diameter of 30 to 40 mm and consisted of layers of SCs; the sheets were approximately 100-μm thick in cross-sectional views (Fig. 1). Approximately 10 sheets were obtained from the 5 g of skeletal muscle.

Implantation of Skeletal Cell Sheets

Autologous SC sheet implantation was performed in the swine 4 weeks after LAD ligation. Swine were anesthetized as mentioned above. The swine were exposed through the sternum. The infarct area was identified visually on the basis of surface scarring and abnormal wall motion. In the SC group, we implanted 10 SC sheets into the infarcted myocardium. The control group was treated similarly but received no SC sheets. Because pilling up four or more sheets caused the central necrosis of the myoblasts presumably because the lack of in oxygen supply, we decided to pile two or three layers of the SC sheet over the broad surface of the impaired heart.

Measurement of Cardiac Function

Swine were anesthetized as mentioned above. Cardiac ultrasonography was performed with a commercially available echocardiograph, SONOS 5500 (PHILIPS Electronics, Tokyo, Japan). A 3-MHz annular array transducer was placed on a layer of acoustic coupling gel that was applied to the left hemithorax. Swine were examined in a shallow left lateral decubitus position. The heart was first imaged in the two-dimensional mode in short-axis views at the level of the largest left ventricle (LV) diameter. The calculation of the LV volume was based on the LV short-axis area using AQ system (*7*). And fractional area shortening (FAS) of the LV diastolic was calculated as follows:

$$\text{FAS}\ (\%)=[(\text{LVend-diastolic area}-\text{LV end-systolic area [ESA]})/\text{LV end-diastolic area}]\times100$$

These data are presented as the average of measurements of two or three selected beats.

Quantification of Regional Diastolic and Systolic Function by Color Kinesis

Diastolic CK images were obtained using a commercially available ultrasound system (SONOS 5500, Philips Medical Systems) from the LV midpapillary short-axis view for the determination of wall motion asynchrony as previously reported (*8*). CK examined every image pixel within the region of interest, which was drawn around the LV cavity, classifying it as blood or tissue based on integrated backscatter data. During diastole, each pixel was tracked into the next frame, and pixel transitions from endocardium to blood were detected and interpreted as diastolic endocardial motions. These pixel transitions were encoded using a color hue specific to each consecutive video frame, so that each color represents the excursion of that segment during a 33-ms period of time. The sites of regional LV diastolic wall motion or regions of interest were set on the basis of standard segmentation models: anterior, lateral, posterior, inferior, anteroseptal wall. The CK diastolic index was defined as the LV segmental filling fraction

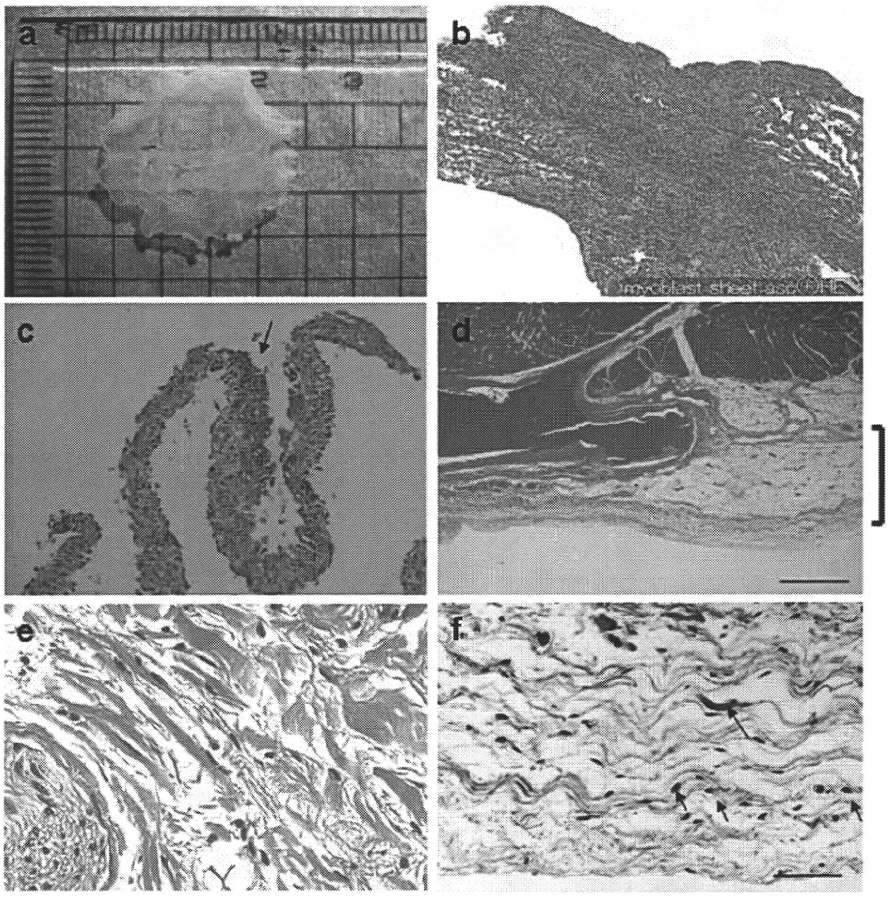

FIGURE 1. Histological characteristics of skeletal cell (SC) sheet. (a) SC sheet detached from the Poly (*N*-isopropylacrylamide)-grafted polystyrene by lowering the temperature. Its size is approximately 3 cm×2 cm^2. (b) Hematoxylin-eosin (H&E) stain; cross-sectional views of SC sheet in vitro. SC sheet demonstrates homogeneous heart-like tissue. (c) Not so many smooth muscle cells were detected in the SC sheets. The *arrow* indicates the smooth muscle cells in the SC sheet. (d) H&E stain revealed that SC sheets attached on the surface of epicardium. *Left square bracket* indicates implanted SC sheets. (e) Oval-shaped cells that showed positive for eosin in cytoplasm were detected in the SC group microscopically in some layers over epicardium. (f) Elastica Masson Goldner showed that oval-shaped cells that supposed to origin from skeletal tissue exist in the transplantation site. *Arrows* indicate oval-shaped cells that suppose to be originated form skeletal tissue.

during the first 30% of the diastolic filling time (LV segmental cavity area expansion during the first 30% of diastole, divided by the segmental end-diastolic LV cavity area expansion, expressed as a percentage). We introduced the use of color kinesis method that displays endocardial motion in real time to evaluate the regional systolic function (*8*).

Histopathology

LV myocardium specimens were obtained 6 months after the SC sheet implantation. Each specimen was fixed with 10% buffered formalin and embedded in paraffin. A few serial sections were prepared from each specimen and stained with hematoxylin-eosin (H&E) stain and elastica Masson-Goldner for histological examination or with Masson's trichrome stain to assess the collagen content.

To label vascular endothelial cells so that the blood vessels could be counted, immunohistochemical staining of factor VIII-related antigen was performed according to a modified protocol. Frozen sections were fixed with a 2% paraformaldehyde solution in phosphate-buffered saline (PBS) for 5 min at room temperature, immersed in methanol with 3% hydrogen peroxide for 15 min, then washed with PBS. The samples were covered with bovine serum albumin solution (DAKO LSAB Kit DAKO CORPORATION, Denmark) for 10 min to block nonspecific reactions. The specimens were incubated overnight with an Enhanced Polymer One-Step Staining (EPOS)-conjugated antibody against factor VIII-related antigen coupled with horseradish peroxidase (DAKO EPOS Anti-Human Von Wille brand Factor/HRP, DAKO, Denmark). After the samples were washed with PBS, they were immersed in diaminobenzidine solution (0.3 mg/mL diaminobenzidine in PBS) to obtain positive staining. Ten different fields at 200× magnification were randomly selected, and the number of the stained vascular endothelial cells in each field was counted under a light microscope. The result was expressed as the number of blood vessels per square millimeter.

The following antibodies against smooth muscle cells and skeletal myosin (slow) were used to evaluate the existence of SCs: primary antibodies, anti-smooth muscle actin (clone 1A4, DAKO) antiskeletal myosin (slow) (clone NOQ7.5.4D, Sigma); secondary antibodies, anti-mouse Ig biotinylate (DAKO).

Picro-sirius red staining for the assessment of myocardial fibrosis or periodic acid-Schiff staining for that of cardiomyocyte hypertrophy was performed as described (*9*).

Positron Emission Tomography Procedure

We performed positron emission tomography (PET) studies on pigs which were transplanted SC sheets and control by using ^{15}0-water and ^{18}F-FDG. The pigs were anesthetized by the introduction of pentobarbital followed by continuous inhalation of propofol (4 mg/kg/hr) and were placed supine on the bed of the scanner. PET was performed using a HEADTOME-III tomograph (Shimadzu, Kyoto, Japan) and data were analyzed as described elsewhere (*10*).

Holter Electrocardiography

To evaluate arrhythmia we used Holter electrocardiography (ECG) for 24 hours. We checked arrhythmia by checking the number of ventricular premature beat after SC sheet implantation in myocardial infarction porcine (n=3).

Data Analysis

Data are expressed as means ± SEM and subjected to multiple analysis of variance (ANOVA) using the StatView 5.0 program (Abacus Concepts, Berkeley, CA). Echocardiographic data were first analyzed by two-way repeated measurement ANOVA for differences across the whole time course, and one-way ANOVA with the Tukey-Kramer posthoc test was used to verify the significant for the specific comparison at each time point. To assess the significance of the differences between individual groups concerning other numeral data, statistical evaluation was performed with an unpaired *t* test. Statistical significance was determined as having a *P* value less than 0.05.

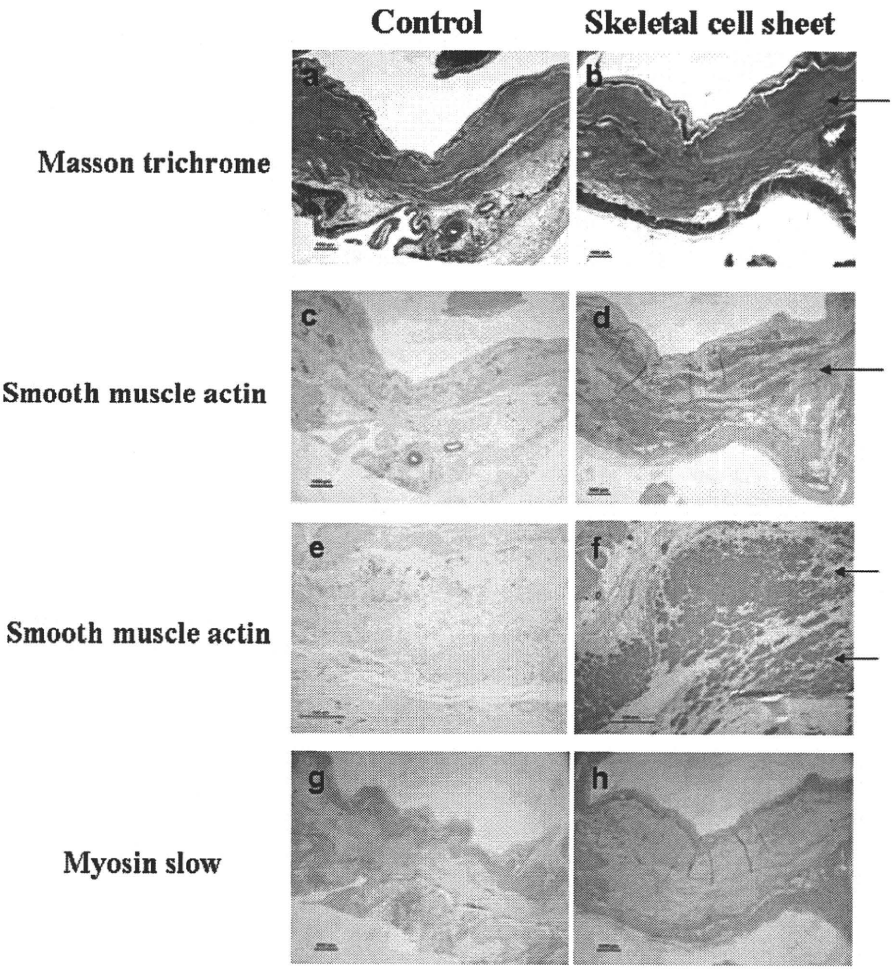

FIGURE 2. The detection of a large quantity of skeletal cells (SCs) in the center of the scar. (a and b) Masson trichrome staining reveals that some layered muscles are detected in the center of the scar in the SC sheet transplantation group, whereas not in the control. (c–f) Smooth muscle actin staining demonstrated that well-developed smooth muscle cells occupied in the center of the scar in the SC sheet transplantation group, whereas only smooth muscle cells which are formed vasculature are detected in the control. (g and h) Slow-type myosin staining showed that no positive cells exist in the center of the scar. This means that SCs which are detected in the center of the scar are not the residual myocyte after infarction.

RESULTS

Characteristics of Myoblast Sheet

We obtained monolayered myoblast sheets by lowering the temperature, which released them from the Poly(*N*-isopropylacrylamide)-grafted polystyrene. Its size is approximately 3 cm×2 cm^2 (Fig. 1a). H&E staining demonstrated that SC sheet contained a lot of SCs and SC sheets had an appearance of homogenous tissue, which thickness of one SC sheet was approximately 100 μm (Fig. 1b). Some smooth muscle cells are detected in the SC sheets, but those cells are not majority (Fig. 1c).

Histological Assessment

H&E staining demonstrated that transplanted SC sheets were attached in the epicardium (Fig. 1d) and oval-shaped cell that showed positive for eosin in cytoplasm were detected in the SC group microscopically in some layers over epicardium (Fig. 1e). Elastica Masson-Goldner showed that oval-shaped cells that supposed to origin from skeletal tissue exist in the transplantation site (Fig. 1f). These cells were not seen in the control group. And the SC group demonstrated decrease in the cross-sectional LV area compared with the C groups (Fig. 2a). Masson's trichrome staining showed that clustered SCs were detected in the center of the scar, whereas clustered SCs were not detected in the C group (Fig. 2a, b). Many clusters of well-developed smooth muscle cells exist in the center of the whole scar in the SC group, whereas in the C group, smooth muscle cells which formed vasculature exist in the scar (Fig. 2c–f). Although slow-type myosin-positive cells exist only on the endocardium and epicardium, those cells were not detected in the center of scar (Fig. 2g,h). So these figures depict that the skeletal muscle cells that exist in the center of the scar is not residual myocyte after infarction.

Quantification of Histopathology

In the SC group, vascular density was found to be significantly higher than in the C groups (SC vs. C=217.1±30.2 vs. 114.2±18.2 /field; $P<0.05$) (Fig. 3b).

Picro-sirius red staining demonstrated that % fibrosis was significantly reduced in the SC group compared with the C group (SC vs. C=1.6±0.2 vs. 3.1±0.3%; $P<0.05$) (Fig. 3b). Periodic acid-Schiff staining showed that cell diameter was significantly shorter in the SC group than the C group (SC vs. C=10.7±0.3 vs. 18.3±1.4 μm; $P<0.05$) (Fig. 3b).

These histological findings were universally identified in the native myocardial tissue without distinction of distance from the grafted region.

Functional Assessment of the Infarcted Myocardium

The FAS and LV end-ESA scores at baseline were not significantly different between the two groups.

Three months after the implantation, two-dimensional echocardiography showed significant improvement of the

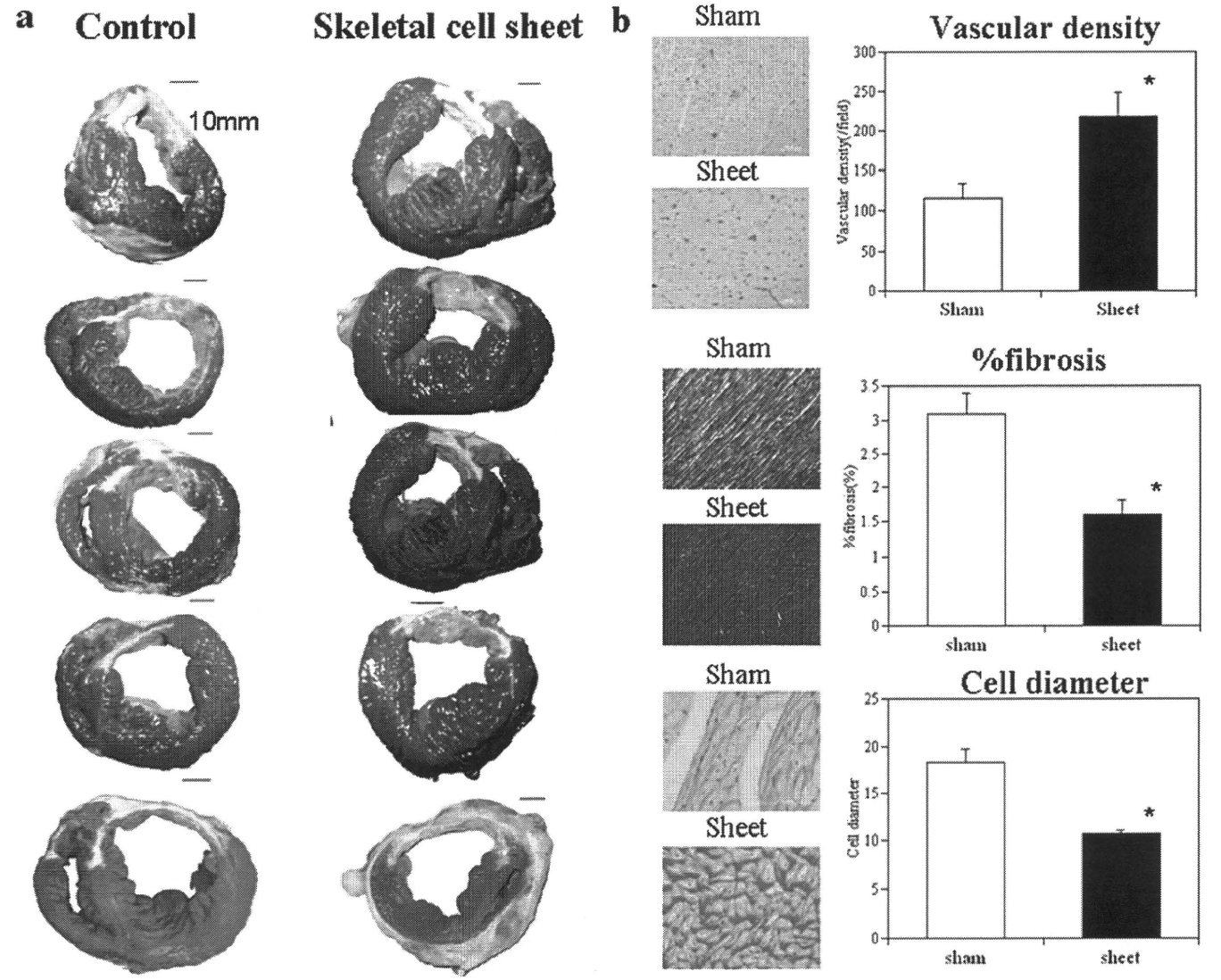

FIGURE 3. Macroscopic images of impaired myocardium receiving skeletal cell (SC) sheets and histological evaluation. (a) In the SC group, the anterior wall has recovered compared with the C group. In the SC group, the short axis area of the left ventricle (LV) is small compared with the C groups. In contrast, the C group shows a dilated LV and the anterior wall is thinner than in the SC groups. (b) Histological evaluation. Vascular density: the SC group showed a significant improvement in vascular density as assessed by immunostaining for the factor VIII-related antigen. *P less than 0.05 vs. C. The ratio of fibrosis-occupied area (% fibrosis) at a site remote from the infarcted heart region: picro-sirius red staining demonstrated that % fibrosis at a site remote from the infarcted heart region was significantly reduced in the SC group compared with the C group. *P less than 0.05 vs. C. The diameter of cardiomyocyte: the diameter of cardiomyocyte is significantly shorter in the SC group than the C group. *P less than 0.05 vs. C.

FIGURE 4. Global functional effects of infarcted myocardium receiving the implant. Global systolic function assessed by the fractional area shortening (FAS) (a) was significantly improved in the skeletal cell (SC) group 3 months after transplantation, and these functional improvements were preserved 6 months after SC sheet implantation. (b) The end-systolic area (ESA) was significantly smaller in the SC group than in the C groups 3 and 6 months after implantation. *P less than 0.05 vs. C, ■: SC sheet, ●: control.

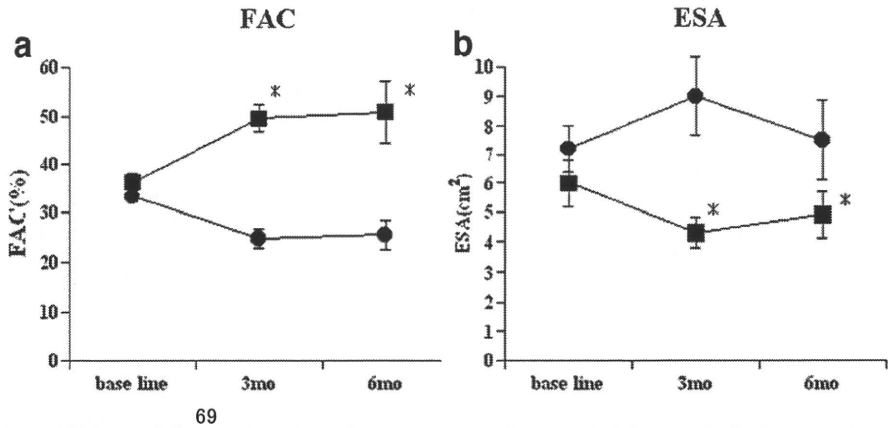

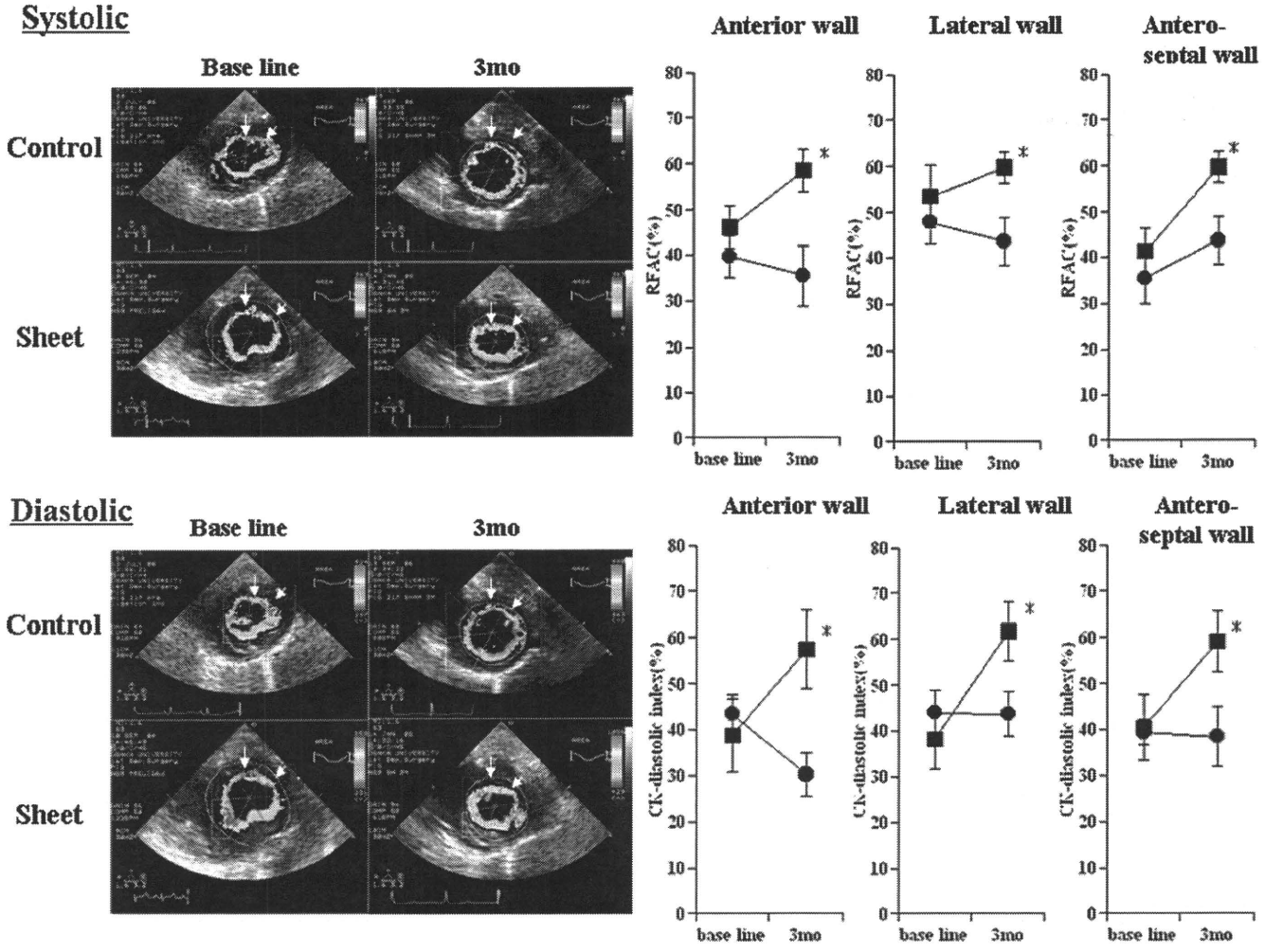

FIGURE 5. Systolic function: regional systolic function was significantly recovered in the skeletal cell (SC) group 3 months after implantation compared with the C group in the anterior, lateral, and anteroseptal wall. *P less than 0.05. Diastolic function: regional dysfunction was significantly recovered in the SC group 3 months after implantation compared with the C group in the anterior, lateral, and anteroseptal wall. Before treatment, diastolic dysfunction was observed in the infarction area of myocardium and the regional delayed relaxation was detected in the remote site of infarction by color kinesis. But this phenomenon was disappeared after SC sheet implantation. *P less than 0.05, ■: SC sheet, ●: control.

FAS (Fig. 4a) in the SC group compared with the C group (SC vs. C=49.5±2.8 vs. 24.6±2.0%, $P<0.05$). These functional improvements were preserved 6 months after implantation (SC vs. C=50.8±6.4 vs. 25.3±2.8%, $P<0.05$). The ESA was significantly smaller in the SC group than in the C group 3 months after the implantation (SC vs. C=4.3±0.5 vs. 9±1.3 cm^2, $P<0.05$) (Fig. 4b). These attenuation of LV dilatation were preserved 6 months after implantation (SC vs. C=4.9±0.8 vs. 7.5±1.4 cm^2, $P<0.05$). During this long-term observation, all SC sheet-treated animals were alive and exhibited no malignant arrhythmia assessed by 24-hour Holter ECG once a week (data not shown).

Before treatment, diastolic dysfunction was observed in the infarction area of myocardium and the regional delayed relaxation was detected in the remote site of infarction by color kinesis. After 3 months after implantation, CK-diastolic index in the lateral (SC vs. C=61.7±6.4 vs. 43.7±4.8%, $P<0.05$), anterior (SC vs. C=57.4±8.6 vs. 30.2±4.7%, $P<0.05$), and anteroseptal (SC vs. C=59±6.6 vs. 38.4±6.6%, $P<0.05$) segment were significantly ameliorated in the SC group compared with the C group, and regional systolic function in transplanted site was significantly improved in the SC group while not in the C groups (SC vs. C: lateral, 59.8±3.3 vs. 43.6±5.4%, $P<0.05$; anterior, 58.5±4.5 vs. 35.4±6.6%, $P<0.05$; anteroseptal, 59.8±3.3 vs. 43.6±5.4%, $P<0.05$), respectively (Fig. 5).

We could detect no ventricular premature beat for 24 hr by the Holter ECG in three myocardial infarction porcine received SC sheets.

Regional Myocardial Blood Flow and Residual Myocardial Tissue

PET study by using ^{15}0-water showed that the myocardial water-perfusable tissue fraction and myocardial blood flow were higher in the anterior wall where SC sheets were implanted compared with the myocardium receiving no sheets. These data depict that myocardial blood flow was better and microcirculation in the infarcted myocardium was preserved in the SC sheets implanted myocardium. PET study by using ^{18}F-FDG revealed that more viable myocardial tis-

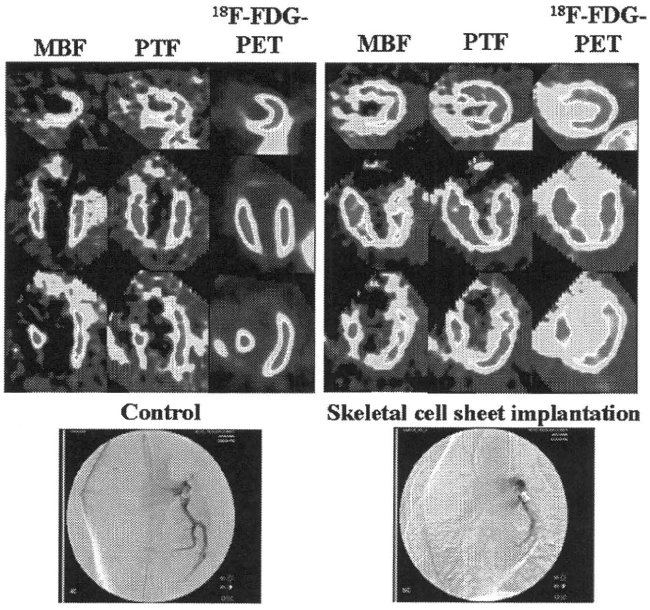

FIGURE 6. Positron emission tomography (PET) study revealed that perfusable tissue fraction (PTF) and myocardial blood flow (MBF) were higher and more viable myocardial tissues were preserved in the skeletal cell sheets implanted site compared with the myocardium receiving no sheets.

sues were preserved in the skeletal sheet implanted myocardium compared with the myocardium receiving no sheets. Coronary angiography revealed that LAD was occluded by the ameroid constrictor in both cases (Fig. 6).

DISCUSSION

Over the past several years, increasing awareness of the shortcomings of heart transplantation and left ventricular assist system implantation has led cardiovascular surgeons to consider alternative means of treating end-stage heart failure. In clinical setting, cellular cardiomyoplasty has been reported to have the potential of fundamental regenerative capability and has already been introduced in clinical trials with skeletal myoblast (*11*) or bone marrow mononuclear cells (*12*), and results suggest that it is a relatively feasible and safety therapy as a therapeutic angiogenesis. In this setting, cardiac tissue implantation was proposed to the treatment of end-staged heart failure as a new concept of regenerative therapy and experimentally some groups depicted it's effectiveness in the damaged myocardium (*13*, *14*). We also reported that cell sheets have great impacts on restoration of damaged myocardium in the rat infarction model (*3*, *4*) and dilated cardiomyopathy hamster (*5*). To convince the effectiveness of cell sheets in preclinical trial, we examined whether autologous SC sheets implantation might become one of the armamentarium of regenerative therapy for chronic heart failure caused by myocardial infarction in the porcine model.

The potential added advantages of the cell sheet implantation method include the implantation of a high number of cells with minimum cell loss. In contrast, the injection method is associated with a high loss of cells or surface proteins due to the trypsin treatment. Despite a high number of cell loss in needle injection, the cell sheet implantation method might provide the advantages of a higher number of cell implantation without cellular community destruction, leading the more improvement of cardiac performance rather than cell injection method (*4*). In case of needle injection, inflammation accompanied with destruction of myocardium induced by needle injection promotes graft death after cell transplantation (*15*).

To examine the effects of the SC sheet implantation therapy, we analyzed cardiac function and performed a histological assessment of the infarcted heart after SC sheet transplantation in a swine infarction model. SC sheet implantation therapy significantly induced angiogenesis, reduction of fibrosis histologically. And cell diameter of host myocyte was significantly attenuated its hypertrophy compared with the no treatment group. PET study revealed the better regional blood perfusion and better regional myocardial viability in the myocardium receiving cell sheets compared with the myocardium receiving no sheets.

Moreover, SC sheet implantation induced functional recovery of damaged myocardium. Especially, we demonstrated that the regional diastolic and systolic dysfunction was well recovered in the sheet implanted group. Before treatment, diastolic dysfunction of infarcted area and regional delayed relaxation of noninfarcted site were detected by color kinesis in the porcine infracted myocardium. After treatment, diastolic dysfunction of infarcted site was significantly recovered and the phenomenon of regional delayed relaxation in noninfarcted site was not seen. Presumably, implanted elastic myoblast sheets and a large quantity of well-developed smooth muscle cells, which are detected in the center of the scar, improved the regional diastolic dysfunction of implanted site. Although SC sheet can not contract in vivo after implantation, this recovery of diastolic disassociation of LV might result in the recovery of systolic dysfunction.

To the best of our knowledge, this is the first report in which tissue-engineered SC sheets implantation was successfully used to improve cardiac performance in a large animal model of ischemic myocardium according to the Laplace's theory.

The mechanisms of the restoration of damaged myocardium by SC sheet implantation might be complicated and many pathways might affect the recovery of ischemic myocardium. Recent reports depict that cell sheets enhance the recruitment of hematopoietic stem cells through the release of stromal-derived factor 1 (*4*). The fact of thicker anterior wall and the improvement of regional function might depend on both the recruitment of cytokine releasing stem cells, survival of grafted cells, and well-developed smooth muscle cells. And these cells might have good elasticity and these elastic cells and tissues softened the stiffness of anterior wall in association with the attenuating fibrosis even in the infarct area. This reduced stiffness of anterior wall might lead to the improvement of the diastolic dysfunction. Transplanted SCs cannot differentiate into cardiomyocyte anymore, but regional systolic function improved in the transplanted site. Probably, the improvement of regional diastolic function due to elastic cells might be responsible for the restoration of regional systolic dysfunction. Recent reports demonstrated that regional left ventricular myocardial relaxation was closely related to regional myocardial contraction (*16*) and the improvement of regional myocardial relaxation leads to the

recovery of global diastolic function (*17*). Moreover, the improvement of regional systolic function is closely related to global systolic function (*18*). We assume that this theory about the relationship between diastolic and systolic function is one of the mechanisms about the improvement of diastolic and systolic function in the cell sheet transplanted myocardium.

Question is why the well-developed smooth muscle cells exist in the center of the scar in the SC sheet group after transplantation despite a small quantity of smooth muscle cells in the SC sheet? Does a small quantity of smooth muscle cells in the SC sheet proliferate after transplantation? Do progenitor cells in the SC sheet differentiate to smooth muscle cells? Do progenitor cells or smooth muscle cells in the host myocardium migrate to the implanted site and proliferate? To the regret, there is no data to answer these questions exactly in this article and more detailed studies are needed to elucidate this important question.

Some reports depicted that the expression of hepatocyte growth factor (HGF) in the myoblast sheet transplanted ischemic myocardium is higher compared with the nontransplanted ischemic myocardium (*4*). HGF has an antifibrotic activity both through the activation of a matrix degradation pathway (*19*), restoration of cytoskeletal proteins on cardiomyocyte (*20*), and induce angiogenesis in the ischemic myocardium (*21*). Our study demonstrated that % fibrosis was significantly reduced in the SC sheet transplanted group. This paracrine secretion of HGF from SC sheets might attribute the reduction of % fibrosis. In our study, much more factor VIII-positive cells are detected in the SC sheet transplanted myocardium. This might be induced by paracrine secretion of HGF and angiogenesis might rescue the ischemic host cardiomyocyte and bring about the improvement of the distressed function of host cardiomyocyte. The distressed cytoskeletal proteins on the cardiomyocyte in the ischemic myocardium might be reorganized by the HGF secreted from skeletal sheet and the restoration of cytoskeletal proteins might lead to the improvement of cardiac function. And some reports demonstrated that myoblast sheets maintain the distressed cytoskeletal proteins on the host cardiomyocyte in the dilated cardiomyopathy hamster model (*5*). Consequently, cell sheet treatment is appropriate for recovery of ischemic cardiomyopathy. Recent research works demonstrated that several regenerative factors such as insulin-like growth factor-1 (*22*) and Thymosin b4 (*23*) were expressed in the rat ischemic myocardium model after myoblast sheet implantation by reverse-transcriptase polymerase chain reaction analysis (data not shown). After myoblast sheet transplantation to ischemic myocardium, several regenerative factors are expressed in the transplanted site, and these long-term and low-dosed expressed regenerative factors might cooperatively restore the damaged myocardium.

We could find no ventricular premature beat analyzed by Holter ECG after SC sheet implantation. We have already proved that in the rat infarction model, arrhythmia is less in the SC sheet implantation group compared with the needle injection group and this work represented that more monocyte chemotactic protein-1-positive cells and CD11b (macrophage marker)-positive cells were detected in the needle injection group compared with SC sheet implantation (data not shown). We speculate that needles destroy the myocardium and this destroyed myocardium may induce the inflammation and this inflammation may induce the arrhythmia. Conversely, SC sheet implantation technique normally doses not destroy the myocardium when they are implanted to recipient heart. Moreover, SC sheet will survive on the epicardium and electrical wave originated from implanted myoblasts may not deliver to the recipient myocardium directly. But when we implant myoblasts by needle injection, implanted myoblasts survive in the center of the myocardium and electrical wave will deliver to the myocardium directly, leading to the arrhythmia.

In conclusion, we have preclinically demonstrated SC sheets produced histologically and functionally apparent prevented the deterioration of the impaired myocardium in the swine model. These data provide a basis for attempting clinical cell sheet implantation in ischemic disease as the armamentarium to promote the regeneration of chronic heart failure caused by myocardial infarction.

ACKNOWLEDGMENTS

The authors thank Shigeru Matsumi and Masako Yokoyama for their excellent technical assistance.

REFERENCES

1. Shimizu T, Yamato M, Akutsu T, et al. Fabrication of pulsatile cardiac tissue grafts using a novel 3-dimensional cell sheet manipulation technique and temperature-responsive cell culture surfaces. *Circ Res* 2002; 90: e40.
2. Shimizu T, Sekine H, Isoi Y, et al. Long-term survival and growth of pulsatile myocardial tissue grafts engineered by the layering of cardiomyocyte sheets. *Tissue Eng* 2006; 12: 499.
3. Miyagawa S, Sawa Y, Sakakida S, et al. Tissue cardiomyoplasty using bioengineered contractile cardiomyocyte sheets to repair damaged myocardium: Their integration with recipient myocardium. *Transplantation* 2005; 80: 1586.
4. Memon IA, Sawa Y, Fukushima N, et al. Repair of impaired myocardium by means of implantation of engineered autologous myoblast sheets. *J Thorac Cardiovasc Surg* 2005; 130: 1333.
5. Kondoh H, Sawa Y, Miyagawa S, et al. Longer preservation of cardiac performance by sheet-shaped myoblast implantation in dilated cardiomyopathic hamsters. *Cardiovasc Res* 2006; 69: 466.
6. Hata H, Matsumiya G, Miyagawa S, et al. Grafted skeletal myoblast sheets attenuate myocardial remodeling in pacing-induced canine heart failure model. *J Thorac Cardiovasc Surg* 2006; 132: 918.
7. Mor-Avi V, Vignon P, Bales AC, et al. Acoustic quantification indexes of left ventricular size and function: Effects of signal averaging. *J Am Soc Echocardiogr* 1998; 11: 792.
8. Ishii K, Miwa K, Makita T, et al. Prolonged postischemic regional left ventricular delayed relaxation or diastolic asynchrony detected by color kinesis following coronary vasospasm. *Am J Cardiol* 2003; 91: 1366.
9. Fukui S, Kitagawa-Sakakida S, Kawamata S, et al. Therapeutic effect of midkine on cardiac remodeling in infarcted rat hearts. *Ann Thorac Surg* 2008; 85: 562.
10. Iida H, Yokoyama I, Agostini D, et al. Quantitative assessment of regional myocardial blood flow using oxygen-15-labelled water and positron emission tomography: A multicentre evaluation in Japan. *Eur J Nucl Med* 2000; 27: 192.
11. Dib N, Michler RE, Pagani FD, et al. Safety and feasibility of autologous myoblast transplantation in patients with ischemic cardiomyopathy: Four-year follow-up. *Circulation* 2005; 112: 1748.
12. Perin EC, Dohmann HF, Borojevic R, et al. Transendocardial, autologous bone marrow cell transplantation for severe, chronic ischemic heart failure. *Circulation* 2003; 107: 2294.
13. Leor J, Aboulafia-Etzion S, Dar A, et al. Bioengineered cardiac grafts. A new approach to repair the infarcted myocardium? *Circulation* 2000; 102(suppl III): III-56.

14. Li RK, Jia ZQ, Weisel RD, et al. Survival and function of bioengineered cardiac grafts. *Circulation* 1999; 100(suppl II): II-63.
15. Suzuki K, Murtuza B, Beauchamp JR, et al. Role of interleukin-1beta in acute inflammation and graft death after cell transplantation to the heart. *Circulation* 2004; 110(11 suppl 1): II-219.
16. Tanaka H, Kawai H, Tatsumi K, et al. Relationship between regional and global left ventricular systolic and diastolic function in patients with coronary artery disease assessed by strain rate imaging. *Circ J* 2007; 71: 517.
17. Tanaka H, Kawai H, Tatsumi K, et al. Improved regional myocardial diastolic function assessed by strain rate imaging in patients with coronary artery disease undergoing percutaneous coronary intervention. *J Am Soc Echocardiogr* 2006; 19: 756.
18. Moller JE, Hillis GS, Oh JK, et al. Wall motion score index and ejection fraction for risk stratification after acute myocardial infarction. *Am Heart J* 2006; 151: 419.
19. Liu Y, Rajur K, Tolbert E, et al. Endogenous hepatocyte growth factor ameliorates chronic renal injury by activating matrix degradation pathways. *Kidney Int* 2000; 58: 2028.
20. Miyagawa S, Sawa Y, Taketani S, et al. Myocardial regeneration therapy for heart failure: Hepatocyte growth factor enhances the effect of cellular cardiomyoplasty. *Circulation* 2002; 105: 2556.
21. Taniyama Y, Morishita R, Aoki M, et al. Therapeutic angiogenesis induced by human hepatocyte growth factor gene in rat and rabbit hindlimb ischemia models: Preclinical study for treatment of peripheral arterial disease. *Gene Ther* 2001; 8: 181.
22. Li Q, Li B, Wang X, et al. Overexpression of insulin-like growth factor-1 in mice protects from myocyte death after infarction, attenuating ventricular dilation, wall stress, and cardiac hypertrophy. *J Clin Invest* 1997; 100: 1991.
23. Bock-Marquette I, Saxena A, White MD, et al. Thymosin beta4 activates integrin-linked kinase and promotes cardiac cell migration, survival and cardiac repair. *Nature* 2004; 432: 466.

Experimental Neurology 223 (2010) 537–547

Contents lists available at ScienceDirect

Experimental Neurology

journal homepage: www.elsevier.com/locate/yexnr

Long-term observation of auto-cell transplantation in non-human primate reveals safety and efficiency of bone marrow stromal cell-derived Schwann cells in peripheral nerve regeneration

Shohei Wakao [a,1], Takuya Hayashi [b,1], Masaaki Kitada [a,1], Misaki Kohama [a], Dai Matsue [a], Noboru Teramoto [b], Takayuki Ose [b], Yutaka Itokazu [c], Kazuhiro Koshino [b], Hiroshi Watabe [b], Hidehiro Iida [b], Tomoaki Takamoto [d], Yasuhiko Tabata [d], Mari Dezawa [a,*]

[a] Department of Stem Cell Biology and Histology, Tohoku University Graduate School of Medicine, Sendai 980-8575, Japan
[b] Department of Investigative Radiology, Advanced Medical Engineering Center, National Cardiovascular Center Research Institute, Osaka 565-8565, Japan
[c] Department of Anatomy and Neurobiology, Kyoto University Graduate School of Medicine, Kyoto 606-8501, Japan
[d] Department of Biomaterials, Field of Tissue Engineering, Institute for Frontier Medical Sciences, Kyoto University, Kyoto 606-8507, Japan

ARTICLE INFO

Article history:
Received 19 November 2009
Revised 25 January 2010
Accepted 29 January 2010
Available online 11 February 2010

Keywords:
Mesenchymal stem cells
Monkey
Schwann cells
Nerve regeneration
Peripheral nerve
Transdifferentiation

ABSTRACT

Based on their differentiation ability, bone marrow stromal cells (MSCs) are a good source for cell therapy. Using a cynomolgus monkey peripheral nervous system injury model, we examined the safety and efficacy of Schwann cells induced from MSCs as a source for auto-cell transplantation therapy in nerve injury. Serial treatment of monkey MSCs with reducing agents and cytokines induced their differentiation into cells with Schwann cell properties at a very high ratio. Expression of Schwann cell markers was confirmed by both immunocytochemistry and reverse transcription-polymerase chain reaction. Induced Schwann cells were used for auto-cell transplantation into the median nerve and followed-up for 1 year. No abnormalities were observed in general conditions. Ki67-immunostaining revealed no sign of massive proliferation inside the grafted tube. Furthermore, ^{18}F-fluorodeoxygluocose-positron emission tomography scanning demonstrated no abnormal accumulation of radioactivity except in regions with expected physiologic accumulation. Restoration of the transplanted nerve was corroborated by behavior analysis, electrophysiology and histological evaluation. Our results suggest that auto-cell transplantation therapy using MSC-derived Schwann cells is safe and effective for accelerating the regeneration of transected axons and for functional recovery of injured nerves. The practical advantages of MSCs are expected to make this system applicable for spinal cord injury and other neurotrauma or myelin disorders where the acceleration of regeneration is expected to enhance functional recovery.

Introduction

Schwann cells are peripheral glial cells that form the myelin of the peripheral nervous system (PNS) and have a major role in neuronal function including saltatory conduction. Following PNS injury, Schwann cells have a pivotal role in axonal degeneration and regeneration. During Wallerian degeneration, myelin is degraded and Schwann cells are activated and proliferate to produce a variety of neurotrophic factors, cytokines, and cell adhesion molecules, thereby providing a pathway for regenerating axons (Fawcett and Keynes, 1990; Hall, 2001; Radtke and Vogt, 2009; Torigoe et al., 1996). Schwann cells have a crucial role in the endogenous repair of the PNS by reconstructing myelin, which is indispensable for neurologic function. Schwann cells also support reconstruction of the injured central nervous system (CNS) where successful axonal regeneration and functional reconstruction are not normally achieved by oligodendrocytes (Dezawa and Adachi-Usami, 2000). Several experiments in the spinal cord and some other areas in the CNS have shown that the injection or transplantation of cultured Schwann cells induces axonal growth across the site of injury and contributes to functional recovery (Bunge, 2002; Bunge, 2008; Hill et al., 2006; Plant et al., 1998; Vukovic et al., 2007). For these reasons, Schwann cells have long attracted attention and are thus one of the most widely studied cell types for axonal regeneration both in the PNS and CNS.

Although Schwann cells have a strong ability to induce nerve regeneration, it is difficult to obtain a sufficient amount of Schwann cells for clinical use. Schwann cell cultivation requires another peripheral nerve being newly sacrificed. In addition, several technical

* Corresponding author. Department of Stem Cell Biology and Histology, Tohoku University Graduate School of Medicine, 2-1 Seiryo-machi, Aoba-ku, Sendai 980-8575, Japan. Fax: +81 22 717 8030.
E-mail address: mdezawa@m.tains.tohoku.ac.jp (M. Dezawa).
[1] These authors contributed equally.

0014-4886/$ - see front matter © 2010 Elsevier Inc. All rights reserved.
doi:10.1016/j.expneurol.2010.01.022